The novel properties of SF_6 for directional dark matter experiments

N. S. Phan[1], R. Lafler, R. J. Lauer, E. R. Lee, D. Loomba, J. A. J. Matthews, E. H. Miller

Department of Physics and Astronomy, University of New Mexico, NM 87131, USA

Abstract

SF_6, an inert and electronegative gas, has a long history of use in high voltage insulation and numerous other industrial applications. Although SF_6 is used as a trace component to introduce stability in tracking chambers, its highly electronegative properties have limited its use in tracking detectors. Here, we present results with SF_6 as the primary gas in a low pressure Time Projection Chamber (TPC), using a thick GEM as the avalanche and readout device. The first results of an ^{55}Fe energy spectrum in SF_6 are presented. Measurements of the drift velocity and longitudinal diffusion confirm the negative ion drift of SF_6. However, the waveform shapes have a peculiar but interesting structure that indicates multiple drift species and a dependence on the reduced field (E/p). The discovery of a distinct secondary peak in the waveform, and its identification and use for fiducializing events in the TPC, are also presented. All of these properties, together with the high spin content of fluorine, make SF_6 a potentially ideal gas for spin-dependent directional dark matter searches.

Keywords: SF_6, negative ion, TPC, Thick GEMs, dark matter, WIMPs

1. Introduction

Sulfur hexafluoride (SF_6) is an inert, odorless, and colorless gas commonly known as an electron scavenger because of its large electron attachment cross-section. The high electron affinity coupled with its non-toxicity and non-flammability make it suitable for use in many practical applications,

[1]Corresponding author

some of which include a gaseous dielectric insulator in high voltage power devices, plasma etching of silicon and Ga-As based semiconductors, thermal and sound insulation, magnesium casting, and aluminum recycling (Refs. [1, 2] provide an extensive review of the properties and applications of SF_6). In particle detectors, SF_6 has been used as a quencher in Resistive Plate Chambers (RPCs) operated in both avalanche and streamer modes, enabling more stable operation by suppressing streamer formation in the former and reducing the energy of discharges and allowing lower voltage operation in the latter [3, 4]. As a result of its many diverse commercial and research applications, SF_6 is one of the most extensively studied gases [1].

Nevertheless, studies of SF_6 in conditions applicable to particle physics detectors other than RPCs are scarce because the qualities that make SF_6 a good insulating gas, namely its electronegativity, also make it a non-ideal primary gas in most detectors due to the difficulty of stripping the electron from the negative ion at the anode, a necessary first step to initiate gas gain amplification. However, with the advent of Micro-patterned Gas Detectors (MPGDs), which have flexible geometries that can sustain high electric fields at low pressures in the avalanche region, the potential for overcoming this barrier could be realized. Demonstrating sufficient gas gain in SF_6 for low energy event detection would open up the possibility for its use in a variety of experiments, such as directional dark matter searches.

The potential for such uses lies in some important similarities with carbon disulfide (CS_2), a negative ion gas that is currently used in the DRIFT directional dark matter experiment [5]. Both SF_6 and CS_2 are highly electronegative with electron affinities of 1.06 eV for SF_6, a value recommended by Ref. [6] based on results from Ref. [7] and Ref. [8], and 0.55 eV for CS_2, the latest and most precise value to date [9]. Note however that, similar to SF_6, the experimentally determined electron affinities of CS_2 have a large spread, ranging from $\sim$ 0.5 - 1.0 eV [10]. Nonetheless, both gases display good high voltage stability at the low pressures ($<$ 50 Torr) necessary for detecting directionality in the low energy nuclear recoils from dark matter interactions.

There are, however, important differences as well. SF_6 has an extremely high room temperature vapor pressure of about 15,751 Torr compared to about 300 Torr for CS_2. In addition, CS_2 is highly toxic and its tendency to be absorbed into detector surfaces make operation and maintenance arduous. Moreover, for spin dependent dark matter searches, neither ^{12}C or ^{32}S atoms have the nuclear spin content to be suitable detection targets whereas ^{19}F is

an excellent one [11]. To circumvent this, the DRIFT experiment employs a mixture of 30/10 Torr CS_2/CF_4, whereby the advantages of the negative-ion CS_2 and the spin content of fluorine can both be utilized. If the potential of SF_6 could be realized, this sacrifice of precious detection volume to the non spin-dependent CS_2 could be avoided, thereby providing a significant improvement to the sensitivity of the experiment.

In addition to its high spin content, the electronegativity of SF_6 is one of the primary characteristics that makes it a potential alternative to CS_2 for use in large-scale tracking detectors. Electronegative gases have played an important role in directional dark matter detection as the world's current leading directional limit is set by the DRIFT IId detector [5], which uses a mixture of CF_4, CS_2 and O_2, with the latter two gases being electronegative. The use of CS_2 in a directional dark matter detector was first suggested by Martoff to suppress diffusion in large-scale detectors without the use of a magnetic field [12]. In a detector with an electronegative gas, the free electrons produced by an ionization event are quickly captured by the gas molecules. The negative ions then undergo thermal diffusion as they drift to the amplification and readout region. The importance of thermal diffusion is that it enables long drift lengths with good tracking resolution, two necessary conditions for track reconstruction experiments and rare event searches that require large detection volumes. Furthermore, electronegative gases tend to display superior high voltage performance over electron drift gases such as CF_4 and N_2 at the low pressures needed for the reconstruction of low energy tracks. In fact, at pressures below about 1 atmosphere, SF_6 has a breakdown field strength that is about three times higher than air [13] and N_2 [14, 15], and because diffusion in the thermal regime scales as $\sqrt{L/E}$, where L is the detector drift length and E is the strength of the drift field, high voltage operation is required for the high fields needed to minimize diffusion over long drift distances. Given the very appealing prospects of SF_6, the questions that we wish to address in this work are:

1. Is it possible to produce avalanche multiplication in SF_6 and detect an ionization signal? This requires the efficient stripping of the electron from SF_6^- in the gain stage.
2. What is the highest achievable gas gain, and how does it depend on pressure? For example, if good gas gain can be achieved at high pressure, it could be of interest in other applications such as the use of SeF_6 (selenium hexafluoride) for double-beta decay searches.

3. What is the diffusion characteristic of SF_6 and how does it compare to CS_2?
4. Is fiducialization of events in the drift direction attainable in SF_6 and/or SF_6 mixtures, and if so, under what conditions?

2. Experimental Setup and Procedure

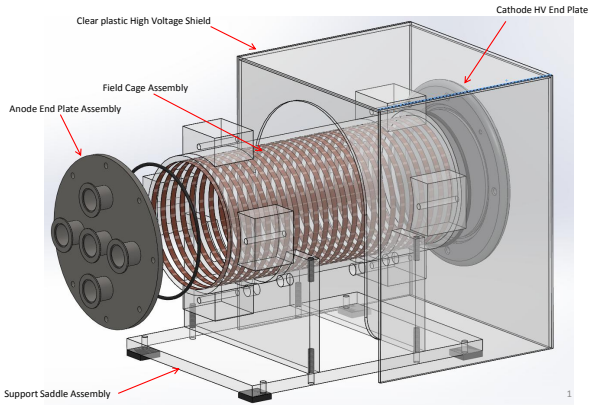

(a) Experimental Setup

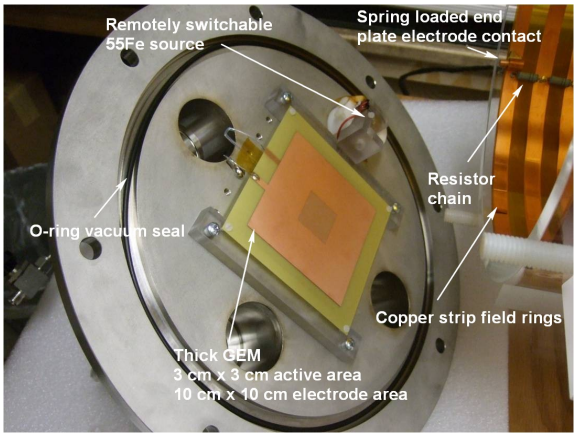

(b) Inner view of anode end plate

Figure 1

The detector used to make measurements for this work is shown in Figure 1 and consists of a 60 cm long acrylic cylinder with an inner diameter of 30.5

cm. The ends of the detector are made from aluminum plates, one of which serves as the cathode, which can be powered up to a maximum voltage of -60 kV. The accuracy of the reading from the front panel meter on cathode power supply has been checked using a FLUKE 289 Multimeter with a high voltage probe. The readings between the two meters are within about 1% at 5 kV and better than 0.1 % at 40 kV so the uncertainty in the cathode voltage should not represent a significant systematic. The other end plate of the vessel is grounded and serves as the anode. The field rings are made from a kapton PC flex board that has 1.3 cm wide copper strips at 1.3 cm spacing and are connected to 23 (56 MΩ) resistors. Amplification is provided by a single 0.4 mm thick GEM (THGEM) with a hole pitch of $\sim$ 0.5 mm that is mounted on two acrylic bars attached to the anode plate. The surface of the THGEM facing the cathode is grounded to the anode plate while the other surface is raised to high voltage. Signals are read out from the high voltage surface with an ORTEC 142 charge sensitive preamplifier which has a 20 ns rise-time (at zero capacitance) and a 100 μs decay time constant.

Ionization can be introduced into the gas volume either from an internally mounted ^{55}Fe 5.89 keV X-ray source (Figure 1b) or by a system using a Stanford Research Systems (SRS) NL100 337.1 nm pulsed nitrogen laser illuminating the cathode. The NL100 laser has a FWHM pulse width of 3.5 ns, a pulse energy of 170 mJ, and a peak power of 45 kW. The spot size in the longitudinal, or drift, dimension is, for our purposes, essentially a delta function, but the projected spot size in the X and Y (lateral) dimensions is a 1 mm x 3 mm rectangle. However, in this paper, we do not make any measurements involving the lateral extent of the ion cloud as it would require wires or readout strips with multiple readout channels.

The operating procedure is as follows: After sealing up the vessel, a weekend long pump down is conducted to reduce out-gassing as much as possible from the acrylic cylinder and other components inside the detector. The vessel is then back-filled with gas to the operating pressure, accurate to 0.1 Torr, and the cathode is powered up to its operating voltage. Noting that although the focus of this paper is on measurements of the basic properties of SF_6, for comparison purposes we also present measurements made in CS_2 using the same setup and operating procedure. Once the cathode is at the full operating voltage, the detector is allowed to sit for about a half-hour to one hour to stabilize before the THGEM is powered up and measurements are made. The measurement waveforms are acquired with a Tektronix TDS 3054C digital oscilloscope and National Instruments data acquisition software

where every triggered event is read out and saved to file for analysis.

The saved files contain the voltage signals from the ORTEC charge sensitive preamplifier which integrates charge collected by the THGEM readout surface with a rise time of $\sim$ 100 ns and an exponential decay time constant of 100 μs. The current, $I(t)$, entering the preamplifier is related to the detected voltage signal, $V(t)$, by

$$I(t) \propto \frac{dV}{dt} - \left(-\frac{V}{\tau}\right), \tag{1}$$

where $\tau = 100$ μs is the decay time constant and the second term is for the decay tail removal. We use Equation 1 to transform the acquired voltage pulses into a current signal in software. After the conversion, pulses are smoothed with a Gaussian filter to suppress high frequency noise. The processed waveforms are then ready for further analysis to measure drift speed, diffusion, and additional features described below.

3. Waveform Features

We measure the drift velocity by firing pulses from the SRS nitrogen laser onto the cathode. The 3.5 ns pulses generate what are essentially point-like ionization events in the longitudinal extent. The laser pulse also provides the trigger to the DAQ system and gives us the initial time marker, T_0. We define the drift time as the time between the initial laser trigger and the arrival time of the pulse peak, T_p, rather than the leading edge of the ionization signal at the THGEM. The magnitude of the drift velocity, v_d, is then given by

$$v_d = \frac{L}{T_p - T_0}, \tag{2}$$

where, $L = 583 \pm 1$ mm, is the distance between the THGEM and the cathode. We measure the drift velocity over a range electric field values (86-1029 V/cm) for several different pressures: 20, 30, 40, 60, and 100 Torr.

The averaged pulse shapes acquired in 20 Torr of SF_6 for six different drift electric field strengths are shown in Figure 2, with zoomed in views in Figure 3. Interestingly, the pulses are not a single Gaussian peak but display additional structure. At low fields, the pulses appear to be a composition of a broad, low amplitude component and a sharp peak. But as the field strength is increased, the relative amplitude and area of the sharp peak (SF_6^-) to that

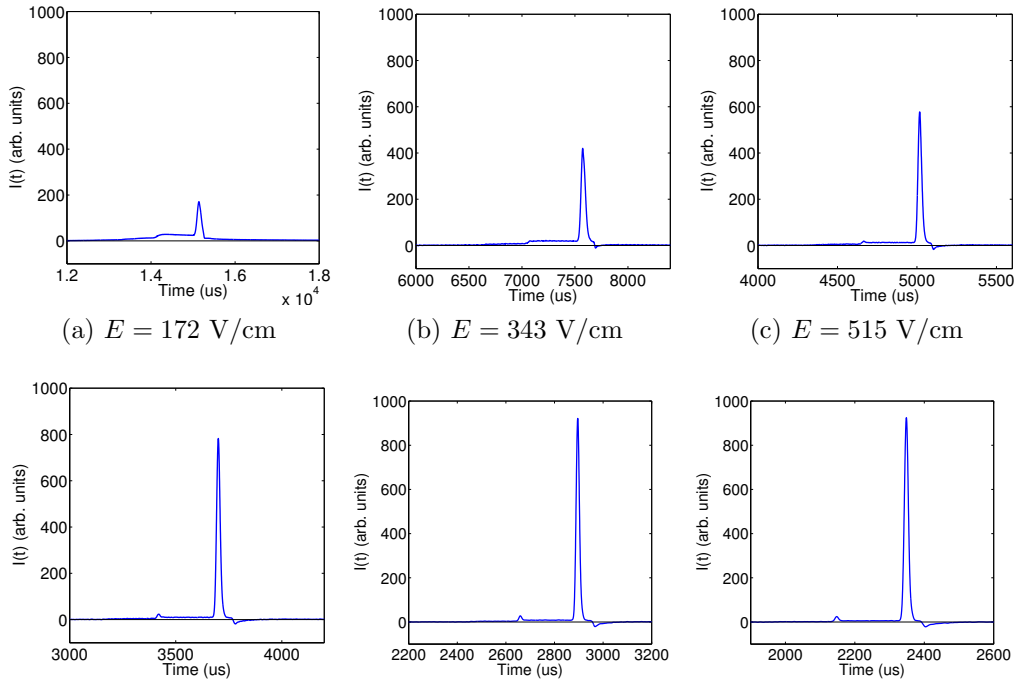

(a) $E = 172$ V/cm (b) $E = 343$ V/cm (c) $E = 515$ V/cm

(d) $E = 686$ V/cm (e) $E = 858$ V/cm (f) $E = 1029$ V/cm

Figure 2: 20 Torr SF_6

of the broad structure also increases. However, this behavior is not only dependent on the field strength but also on the pressure as well, and is not a simple reduced field (E/p or E/N) effect. The pulse shapes from the 30, 40, 60, and 100 Torr SF_6 data acquired with $E = 1029$ V/cm are shown in Figure 4. Besides the positive valued features, in each of Figures 2b - 2f, a small amplitude dip arriving after the primary peak is observed. This feature has to do with the way the THGEM is connected. The surface of the THGEM facing the cathode and opposite the readout surface is grounded to the anode lid. Positive ions produced from the avalanche will drift away from the positive voltage readout surface and towards the grounded THGEM surface as well as the anode ground. The ions induce a small positive signal as they move away from the readout surface but then a small negative signal is induced as the ions approach the grounded anode end plate. This is because one of the THGEM surfaces is connected to the anode but is capacitively coupled to the readout surface.

Explanations for the rich structures shown in Figures 2, 3, and 4 and their dependence on the drift field and gas pressure lie in the complex chemistry associated with electron capture and drift in SF_6 [REFs]. Although modeling of the detailed shape of the waveform is beyond the scope of this work, here we discuss some of the chemistry that could describe some of the gross features. However, as will become clear below, a full understanding of the mechanisms leading to the observed structures eludes us at present.

Measurements made under differing conditions have shown that electron capture by the electronegative SF_6 occurs very quickly [REFs], with the immediate product being SF_6^{-*}, a metastable excited state of the anion, SF_6^-, which is subsequently formed from the collisional or radiative stabilization of the excited state [2]. The electron capture cross-sections by SF_6 are very large and estimates of the capture mean-free-path are of order XXX at the pressures and drift fields of our experiments. The metastable SF_6^{-*} leads to subsequent products, besides SF_6^-, whose relative abundance depends on the lifetime of SF_6^{-*}, the electron energy, gas pressure, and drift field:

$$SF_6 + e^- \rightarrow SF_6^{-*} \qquad \text{(attachment, metastable)} \tag{3}$$

$$SF_6^{-*} \rightarrow SF_6 + e^- \qquad \text{(auto-detachment)} \tag{4}$$

$$SF_6^{-*} + SF6 \rightarrow SF_6^- + SF_6 \qquad \text{(collisional stabilization)} \tag{5}$$

$$SF_6^{-*} \rightarrow SF_5^- + F \qquad \text{(auto-dissociation)} \tag{6}$$

Under collision-free conditions, time-of-flight (TOF) mass spectrometric experiments indicate the lifetime for autodetachment (4) to be between 10 - 68 μs [16, 17, 18, 19, 20, 21]. Measurements made with ion cyclotron resonance (ICR) experiments indicate the lifetime of the metastable SF_6^{-*} ion to be in the ms range [22, 23, 24]. The difference in the measured liftetime between the two techniques has to do with the experimental conditions. Specifically, the electron energies in ICR experiments are usually much lower than in TOF experiments [2]. For our experimental conditions, the mean-free path, λ, which can be estimated from the measured drift speed by

$$\lambda = \frac{(3MkT)^{1/2}\, v_d}{eE} \tag{7}$$

[25], where $T = 296$ K and M is the mass of the SF_6 molecule, is $\sim 0.1 - 1$ μm, implying a collisional mean-free time of $\sim 1 - 10$ ns. But note that the average time between collisions is not necessarily the stabilization time.

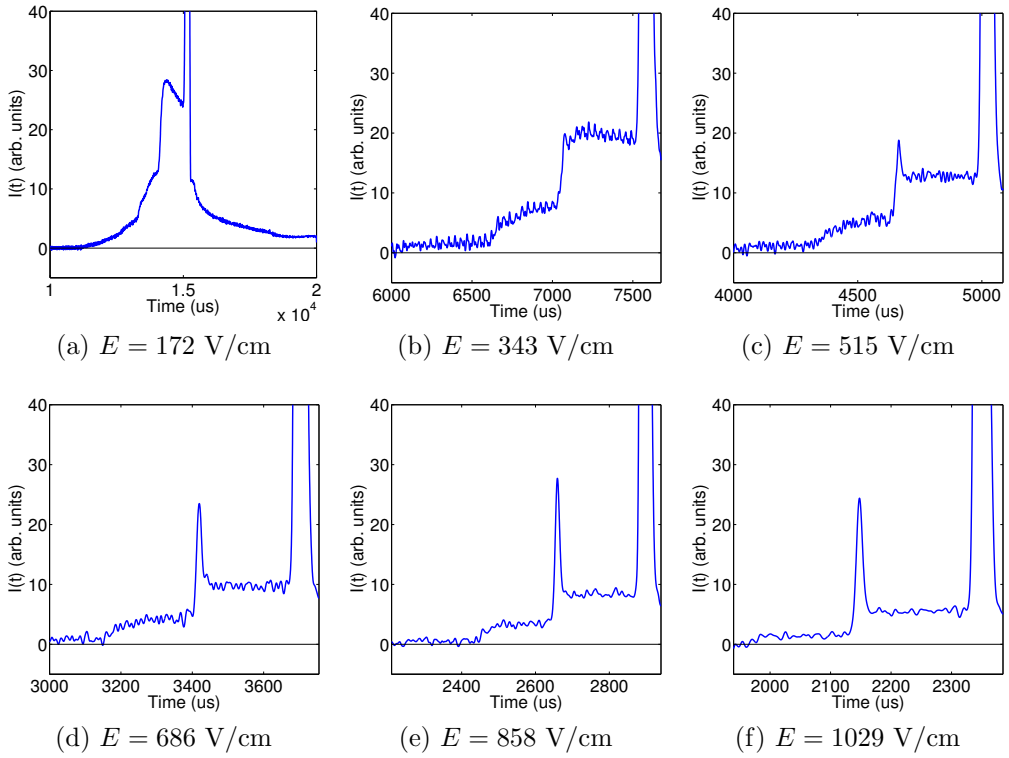

(a) $E = 172$ V/cm (b) $E = 343$ V/cm (c) $E = 515$ V/cm

(d) $E = 686$ V/cm (e) $E = 858$ V/cm (f) $E = 1029$ V/cm

Figure 3: 20 Torr SF_6, close up view of pre-primary peak ionization.

Reactions leading to the production of F^- and SF_4^- also occur but at higher electron energies and with significantly lower probability [26, 27, 28, 29], thus, we ignore them in the following discussion but return to them below. The cross-section for reaction (4) is peaked at zero electron energy [29, 30, 31, 33], falling by a factor of about 100 at 0.1 eV [28, 29, 32], whereas that for reaction (6) has a peak at 0 eV [32] and a smaller one at ~ 0.38 eV [28, 29, 32], with the former smaller by a factor 1000 than that for SF_6^-. Therefore, at the low electron energies expected in our experiments, SF_6^- should be the dominant charge carrier arriving at the cathode; i.e., $SF_6^-/SF_5^- > 10$. Because of the higher mobility of SF_5^- ([34, 35, 36], and see Section 4 below) we should detect two peaks at the anode, with the faster SF_5^- arriving earlier

in time. However, a number of possible reactions occurring at the start and during drift complicate this simple picture.

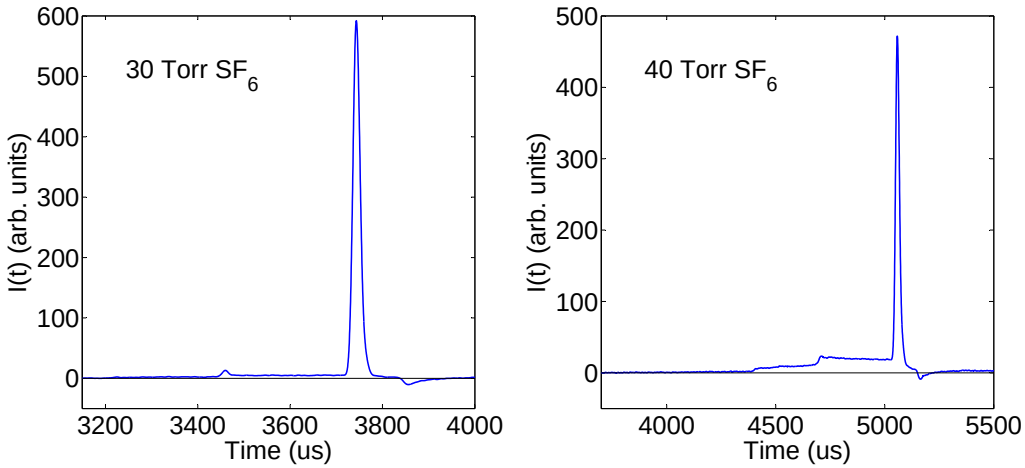

(a) 30 Torr

(b) 40 Torr

(c) 60 Torr

(d) 100 Torr

Figure 4: Average waveforms for 30, 40 , 60, and 100 Torr at $E = 1029$ V/cm.

At the cathode where electrons are generated and first captured to form SF_6^{-*}, auto-detachment (4) will compete with reactions (5) and (6) until all SF_6^{-*} is depleted, with only stable SF_6^- and SF_5^- remaining. The degree to

which this contributes to the pulse-shape will depend on the lifetime of SF_6^{-*} and the mean-free-time for collisional stabilization which are both dependent on the the pressure and drift field. If a significant fraction of the initially produced SF_6^{-*} auto-detaches, the free electrons will be re-captured quickly, and the process will repeat until SF_6^{-*} is fully depleted via reactions (5) and (6). If the electron capture mean-free-time is indeed very short, the waveform detected at the anode is due purely to the negative ions SF_5^-, SF_6^- and SF_6^{-*} drifting in the chamber. If in addition we assume that the mobilities of SF_6^{-*} and SF_6^- are equal, the waveform would consist of two peaks with structure in between due to the initial phase of attachment/auto-detachment. Specifically, the main SF_6^- peak is the fraction of initially produced SF_6^{-*} that eventually converts to SF_6^-, and the region between it and the SF_5^- peak is from SF_6^{-*} undergoing numerous attachments/auto-detachments, (3) and (4), before finally auto-dissociating to SF_5^- via (6) . The latter arrives between the SF_5^- and SF_6^- peak because its drift velocity is a weighted average between that of SF_6^{-*} and SF_5^-. A key point here is that a significant initial phase of attachment/auto-dissociation will result in a larger fraction of SF_5^- arriving at the anode. Thus, the SF_5^-/SF_6^- ratio is, with all else equal, governed by a competition between the probability of auto-detaching relative to collisional stabilization, (5). The mean-free-time for the latter process should decrease with increasing drift electric field, resulting in higher SF_6^- fraction. As we show below, this model does explains some of our data.

A fuller picture, however, must also account for possible interactions engaged by the SF_5^- and SF_6^- during the ~ 60 cm drift to the anode. At low drift fields, neutral, electron-hungry SF_6 molecules will form clusters around the negative ions [REFs]. This has been observed by others, but with measured mobilities that are lower for the resulting drifting $SF_6^-(SF_6)_n$ and $SF_5^-(SF_6)_n$ $(n = 1, 2, 3, ...)$ clusters than those of SF_5^- and SF_6^- [REFs]. This phenomena could therefore explain the long tail on the slow side of the SF_6^- peak of our low field pulse-shapes shown in Figures 2a and 3a and the low reduced field pulse-shape in Figure 4d. In addition to clustering, the drifting SF_5^- and SF_6^- could also interact with the neutral gas leading to other species [REFs]. Importantly, the probability of collisional detachment of energetically stable SF_5^- and SF_6^- via the following reactions:

$$SF_5^- + SF_6 \rightarrow SF_5 + SF_6 + e^- \qquad \text{(collisional detachment)} \qquad (8)$$

$$SF_6^- + SF_6 \rightarrow SF_6 + SF_6 + e^- \qquad \text{(collisional detachment)} \qquad (9)$$

is very small for center-of-mass energies < 60 eV [37]. In comparison to the electron affinities of SF_5 ($2.7 - 3.7$ eV) [38] and SF_6 (1.06 eV), the threshold for detachment is much larger and is attributed to competing charge-transfer and collision-induced dissociation processes [37, 39, 40]. However, there is evidence that energetically unstable states of SF_6^- (i.e. SF_6^{-*}) can contribute to collisional detachment [37, 39]. The relative contributions of these effects depend on the interaction energies at different reduced electric fields.

With this overview of the chemistry of electron drift in SF_6, we turn to a detailed look at our data shown in Figures 2, 3, and 4. Figures 2 and 3 show the evolution of the pulse-shapes at $P = 20$ Torr ($N = 6.522 \times 10^{17}$ cm^{-3} at $T = 296$ K) as a function of drift field, and Figure 4 shows the evolution at a fixed drift field, $E = 1029$ V/cm, as a function of pressure. Both figures show a complex structure at low reduced fields that evolves to a simpler one at high reduced fields. At the highest reduced fields (Figures 2e, 2f, 3e, 3f, and 4a) two peaks are clearly seen, with some charge in between and a smaller amount arriving faster than the secondary peak. The larger, lower mobility peak is SF_6^- and the smaller secondary peak is attributed to SF_5^-. To interpret how the waveform evolves with reduced field we consider Figure 4 first. Naively, we would expect that increasing gas density at a fixed E would result in a shorter mean-free-time between collisions, allowing more of the SF_6^{-*} to stabilize to SF_6^- at the expense of auto-detachment. The shorter mean-free-times with increasing pressure would also argue for lower electron energies, resulting in more SF_6^- relative to SF_5^-. What is observed instead is a relative increase of charge carriers with higher mobility than SF_6^-, implying an increase in auto-detachment, SF_5^-, or other species. The structure seen in the pulse-shape in this regime, and its evolution with pressure shown in Figure 4, is not understood at this time.

The evolution of the waveform as a function of drift field at fixed $P = 20$ Torr (Figures 2 and 3), however, is better fit with the model outlined above. There we suggested that increasing E (for fixed P) should lead to shorter mean-free-times for collisional stabilization, (5), shifting the inter-peak charge (attributed to SF_5^-) into the SF_6^- peak. But the increase in electron energy expected at higher E should, if significant, also result in an overall increase in the SF_5^- fraction. Therefore, the charge lying between the SF_5^- and SF_6^- peaks at low E, which was due to SF_5^- produced at the end of numerous SF_6^{-*} auto-detachment reactions (4), as surmised above, will move into the main SF_6^- peak at high E. The data in Figures 2 and 3 do show a decrease in the inter-peak charge region and, starting at $E = 515$

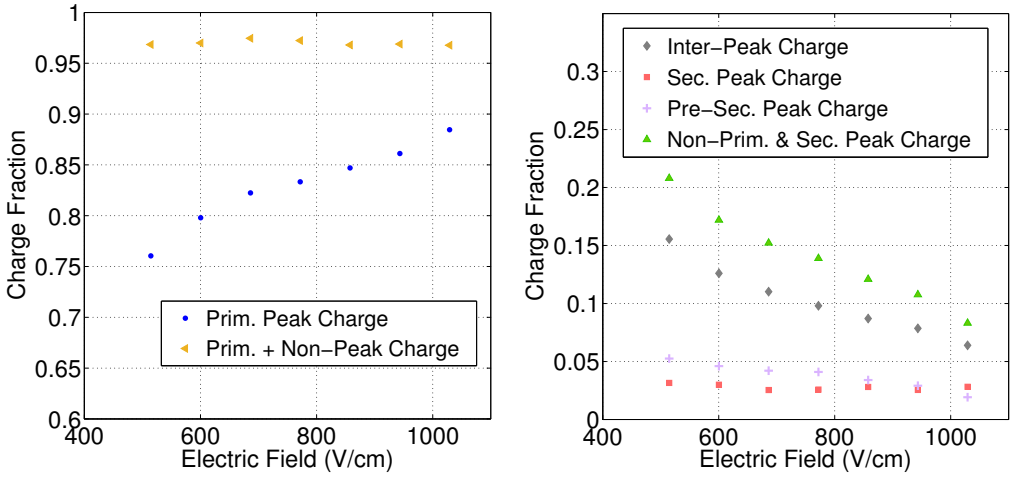

(a) Charge Fraction (b) Charge Fraction Low

Figure 5: The fractional charge contained in different parts of the waveform in 20 Torr SF_6 as a function of the electric field. The primary and secondary peaks correspond to the SF_6^- and SF_5^- peaks, respectively.

V/cm, an SF_5^- peak begins to emerge (clearer in the zoomed in Figure 3c). By $E = 1029$ V/cm (Figures 2f and 3f) nearly all of the charge carriers are in the SF_5^- and SF_6^- peaks, with only a small fraction lying in between. Although Figure 3c-3f indicates that SF_5^- grows with E, as expected from our simple model, a more quantitative assessment is required.

To study this we average 200 waveforms for each of seven different electric field strengths between 515-1029 V/cm, all at fixed $P = 20$ Torr. The resulting averaged waveforms are divided into four regions, from left to right: the pre-SF_5^- peak region, the SF_5^- peak, the area between the SF_5^- and SF_6^- peaks, and the SF_6^- peak. The evolution of the fraction of charge in each region as a function of the electric field is shown in Figure 5. As predicted by our simple model, essentially all of the inter-peak charge appears to shift over into the SF_6^- peak. However, there is no detectable change in the SF_5^- peak, which suggests only a small, if any, increase in electron energies with the drift field.

A final puzzle in our data is the charge seen on the higher mobility side of SF_5^-. This is clearly seen in Fig. 3b-3f and, like the inter-peak charge, it too decreases with electric field. The fact that this charge has an edge on the left side, i.e., a minimum drift time, implies another electronegative species

produced with a similar mechanism to SF_5^- that competes with collisional stabilization, (6), to SF_6^-. The mobility of the charge arriving at this edge is plotted in Figure 6 of Section 4. As mentioned above, SF_4^- and F^- are also produced as in (6) for SF_5^-, but with much lower probabilities. These are both good candidates to explain this feature but unfortunately only the F^- mobility has been measured (see Section 4), and it does not agree with ours. Suffice it to say, a full understanding of all the processes involved in the evolution of the waveforms seen in Figures 2-4 requires further study. For the purposes of this work, we focus on the main SF_5^- and SF_6^- peaks and their use in dark matter experiments.

4. Mobility

The mobility, μ, of a drifting ion at a specific gas density is related to the drift speed and electric field through the relation,

$$v_d = \mu \cdot E, \tag{10}$$

where E is the electric field. By convention, rather than reporting μ or v_d, the reduced mobilities, μ_0, are reported instead as determined from the formula

$$\mu_0 = \frac{v_d}{E}\frac{N}{N_0}, \tag{11}$$

where $N_0 = 2.687 \times 10^{19}$ cm^{-3} is the gas density at STP (0°C and 760 Torr) and N is the detector gas density at the time of measurement. Mobilities for several negative ion species as a function of the reduced field (E/N) in units of the Townsend (1Td = 10^{-17} V cm^2, 1 V cm^{-1} Torr^{-1} = 3.066 Td at $T = 296$ K) are plotted in Figure 6. We find good agreement for the reduced mobility of CS_2^- in CS_2 in the low field regime (< 50 Td) between our results and that reported by Ref. [41]. For SF_5^- and SF_6^- in SF_6, excellent agreement is found with the mass-identified mobility measurements reported in Ref. [35] over the full range of our data set. A comparison of our mobilities and those from Ref. [35] with mobilities reported in Ref. [34] shows agreement only for reduced fields less than $\sim$ 60 Td for both SF_5^- and SF_6^-. The same comparison with Ref. [36] shows good agreement for SF_6^- over the full range of the data set but only up to about $\sim$ 60 Td for SF_5^-.

In addition to the mobilities for CS_2^-, SF_5^- and SF_6^-, Figure 6 also contains the mobilities for possibly another negative ion drifting in SF_6, which we label

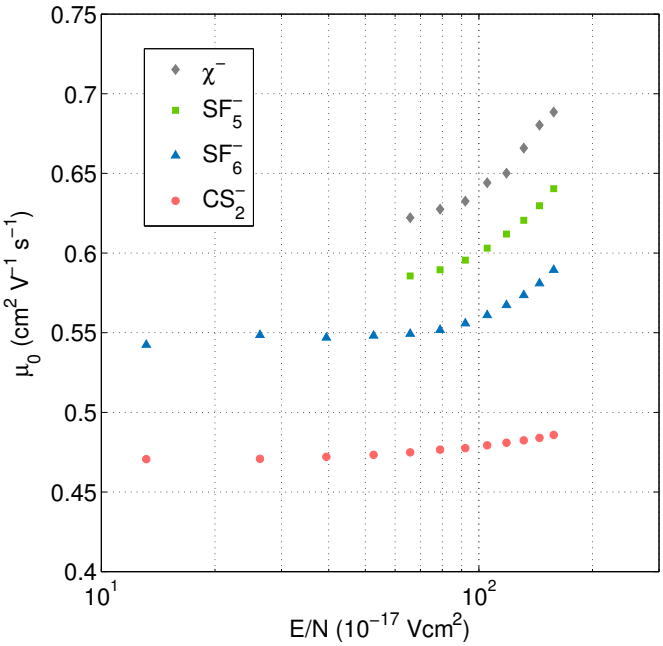

(a) Reduced mobilities in SF_6 and CS_2

Figure 6: The reduced mobilities as a function of reduced field for χ^-, SF_5^-, and SF_6^- in SF_6 and CS_2^- in CS_2. The SF_5^- and χ^- mobilities only go down to $\sim$ 66 Td because the peak and feature becomes difficult to identify at fields lower than this value. Our results for SF_5^- and SF_6^- are in excellent agreement with those found in Ref. [35] while the CS_2^- results agree with the result of Ref. [41].

χ^-. The presence of this species is most clearly seen in Figures 3d and 3e as small steep edges arriving before the SF_5^- peak at $\sim$ 3150 and 2450 μs, respectively. The χ^- mobility is far lower than the reported mobility for F^- in SF_6^- [42] but is very close to the mobilities reported for the positive ions SF_3^+ and SF_4^+ [43, 44]. This is interesting because of the remarkable similarity found between the mobilities of SF_5^+ and SF_5^- [35, 44], which could suggest similar behavior for the positive and negative ions of SF_3 and SF_4. But at the same time, this is unexpected because the cross-section for F^- production is higher than that for SF_3^- and SF_4^- [REF]. Nevertheless, even at the highest reduced field, there is no identifiable peak for χ^-, so it is also possible that it is not actually another negative ion species in SF_6 but is rather only a feature resulting from the processes responsible for the production and transport of SF_5^- and SF_6^- in the gas. Intriguingly, the mobility for this unidentified

species (or feature) is closely matched with the reported mobility for SF_5^- in Refs. [34] and [36] for reduced fields above $\sim$ 70 Td, and at the same it is worth noting that the majority or all of the data from Refs. [34] and [36] do not have mass analysis.

For a reduced field less than 60 Td, the CS_2^- mobility is about 13.7% lower than SF_6^- mobility, but this difference rises to about 17.6% at about 158 Td which shows that SF_6^- mobility increases more rapidly with reduced field than CS_2^- mobility. This is quite interesting because SF_6, as compared to CS_2, is a much heavier molecule and the drift velocity for ions with mass, m, drifting in a gas with molecules of mass, M, follow the formula,

$$v_d = \left(\frac{1}{m} + \frac{1}{M}\right)^{1/2} \left(\frac{1}{3kT}\right)^{1/2} \frac{eE}{N\sigma}, \tag{12}$$

where σ is ion-gas molecule cross-section [45]. This, of course, implies that the cross-section for SF_6^-:SF_6 interaction is lower than that for CS_2^-:CS_2 interaction. Comparing the mobility of SF_5^- to SF_6^-, we see that the mobility of the former is 6.6% higher than the latter at about 66 Td and is 8.7% larger at about 158 Td which would indicate that SF_5^- mobility increases more rapidly with reduced field. At reduced fields of about 66 Td and 158 Td, the χ^- feature is 13.3% and 16.8% faster than SF_6^-, respectively.

It is interesting to note that the behavior of the mobility with reduced field for the negative ions in Figure 6 is in stark contrast to positive ion drift in noble gases where the drift velocity is proportional to E at low fields, which is to say that the mobility is independent of E, but becomes proportional to $\sqrt{E}$ at high fields, or that the mobility decreases as $1/\sqrt{E}$ [45]. Of course, the behavior of negative ion drift is complicated by the process of electron capture as well as other processes such as ion-conversion occurring during transport. The capture cross-section is strongly dependent on the electron energy, and in the case of SF_6^-, is maximal near zero-energy but decreases with increasing electron energy [29, 30, 31, 33]. The transport processes are also energy dependent as can be seen with the rise in mobility with increasing reduced field for all of the negative ions in Figure 6. This has important implications for diffusion at high reduced fields as we show in Section 5.

5. Longitudinal Diffusion

At small field strengths where the diffusing charge cloud has thermal energy, the diffusion coefficient at zero E/N, $D(0)$, is related to the mobility

and temperature through the Nernst-Townsend-Einstein relation:

$$\frac{D(0)}{\mu(0)} = \frac{kT}{e}, \tag{13}$$

[46]. At higher field strengths, approximate relations known as the generalized Einstein relations (GER) have the form,

$$\frac{D_L}{\mu} = \frac{kT_L}{e}\left[1 + K^{'} + \Delta_L K^{'}\right] \tag{14}$$

$$\frac{D_T}{\mu} = \frac{kT_T}{e}\left[1 + \frac{\Delta_T K^{'}}{2 + K^{'}}\right], \tag{15}$$

where $K^{'}$ is the field derivative of the mobility, defined as

$$K^{'} = \frac{d\ln\mu_0}{d\ln(E/N)} = \frac{E/N}{\mu_0}\frac{d\mu_0}{d(E/N)} \tag{16}$$

and Δ_L and Δ_T are correction terms with magnitude ranging from 0 to 0.20 for the longitudinal and transverse diffusion coefficients D_L and D_T, respectively [47]. However, for this section we will use the expression for the diffusion coefficient in the zero field approximation given by Eq. 13. With that relation, a starting point-like charge cloud drifting over a distance, L, has a longitudinal diffusion width, σ_z, given by

$$\sigma_z^2 = 2D_L t = \frac{4\epsilon L}{3eE} = \frac{2kTL}{eE}, \tag{17}$$

where $t = L/v_d$ and $\epsilon = 3/2kT$ [45]. The diffusion in the time domain, σ_t, is converted to a spatial width by the simple relation,

$$\sigma_z = \sigma_t \cdot v_d. \tag{18}$$

Customarily, diffusion is expressed by normalizing the measured value relative to the drift length:

$$\sigma_0 = \frac{\sigma_z}{\sqrt{L}} = \sqrt{\frac{2kT}{eE}}, \tag{19}$$

where σ_0 has units of $\mu\text{m}/\sqrt{\text{cm}}$.

At each pressure and electric field, one hundred pulses are averaged to increase signal-to-noise before fitting to a Gaussian curve. The diffusion width, $\sigma_{\rm t}$, is found by subtracting, in quadrature and assuming no correlation, all other contributions from the fitted width, $\sigma_{\rm fit}$. For us these are the electronics shaping time, $\sigma_{\rm smooth}$, laser spot size, $\sigma_{\rm spot}$, electron-capture mean-free-path, and possible effects at the THGEM. In our measurements, the laser spot size contribution to the longitudinal width is negligible, but the latter two effects are not. However, we do not have the ability to determine the capture mean-free-path and the THGEM effects, so they are left out of the quadrature subtraction in Eq.20 but will be included as systematics with estimates of their values given below:

$$\sigma_t = \sqrt{\sigma^2_{\rm fit} - \sigma^2_{\rm smooth} - \sigma^2_{\rm spot}}. \tag{20}$$

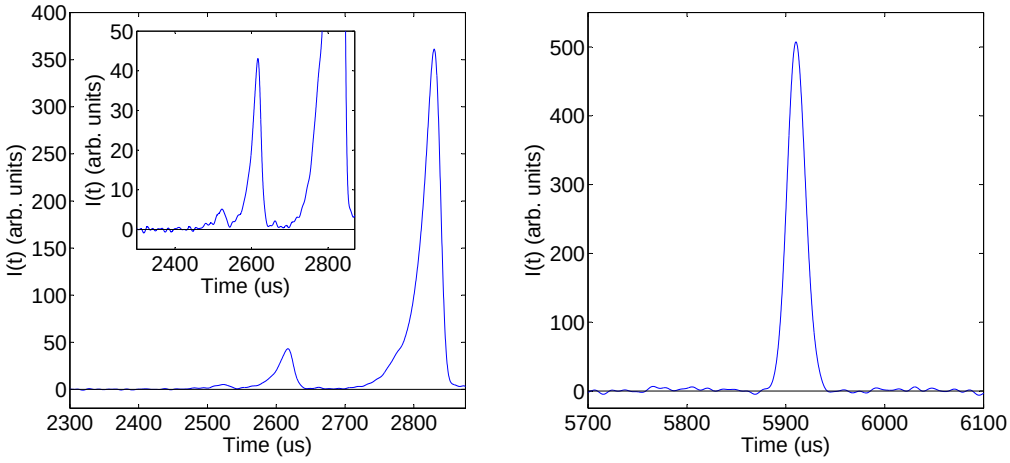

(a) CS_2 20 Torr Averaged Waveform (b) CS_2 40 Torr Averaged Waveform

Figure 7: (a) The averaged waveform for 20 Torr CS_2 at $E = 1029$ V/cm showing the presence of a large secondary peak at ~ 2600 μs and the possible appearance of two additional peaks at ~ 2660 μs and ~ 2520 μs (inset). In addition, the distortion in the waveform shape is clearly seen in both the primary and secondary peaks at this high reduced field. (b) The average waveform for 40 Torr CS_2 at $E = 1029$ V/cm which shows no clear secondary peaks or distortion in waveform shape.

Besides the systematic effects, the quadrature subtraction could also be a source of bias because the pulse width is not truly Gaussian, but appears

to exhibit a tail on the right side due to an induced signal caused by ions drifting away from the THGEM readout. The ion tail is a feature that is also observed in [41]. To exclude the induced signal, we fit only the left hand side of the pulse up to the peak. Besides the long ion tail, we showed in Section 3 that the pulses in SF_6 contain additional structure that tends to grow with decreasing reduced field, making it difficult for fitting. Thus, we only fit the data for $E > 500$ V/cm at 20 Torr and $E = 1029$ V/cm at 30 and 40 Torr. By performing multiple fits of the waveform with different smoothing widths, we estimate that the error introduced by subtracting the smoothing width, σ_{smooth}, to be about XX mm.

For a comparison, we also fit the 40 Torr CS_2 data (Figure 7b) but not the 20 Torr data because of distortion in the waveform at high fields (Figure 7a). The smaller, secondary peak at ~ 2600 μs in Figure 7a is a new feature discovered here, which could be another species of negative ion in CS_2 (e.g. CS^- produced similarly to SF_5^- via auto-dissociation (Eq.6) that is created at high reduced fields. This secondary feature first appears at a drift field of $E = 343$ V/cm at 20 Torr CS_2 and has a drift speed that is $\sim 6.2\%$ faster than, and an amplitude only 0.4% that of the primary peak value. When the drift field is increased to $E = 686$ V/cm, the secondary peak's drift speed and amplitude increase to 6.8% and 4.6%, respectively, relative to that of the primary peak. Finally, at $E = 1029$ V/cm, the secondary peak is about 7.5% faster than the primary while its amplitude continues to grow and reaches about 11.7% of the primary's peak value (Figure 7a).

The results for $E = 1029$ V/cm are shown in Table 1. The second column contains widths where no attempt was made to subtract non-diffusion related contributions from σ_z, which are discussed below. At 40 Torr $SF_6(CS_2)$, the value of $\sigma_z = 0.74(0.73)$ mm corresponds to a temperature of 556(541) K. This is of course much higher than the ambient room temperature and an expected σ_z of 0.54 mm for thermal diffusion, but is not surprising due to the neglected contributions to pulse width mentioned above.

The two possible main sources of systematics contributing to the pulse width are the electron-capture mean-free-path and distortions in the uniformity of the drift field due to the dipole contributions from the holes in the THGEM. Here we place bounds on the sum of these contributions. For CS_2, the capture distance could be as large as 0.35 mm in 40 Torr [41], but we do not know this value for SF_6. By subtracting in quadrature the expected σ_z and the capture length from the measured value of 0.73 mm in 40 Torr CS_2, we estimate that the lower bound on the systematic could be at least

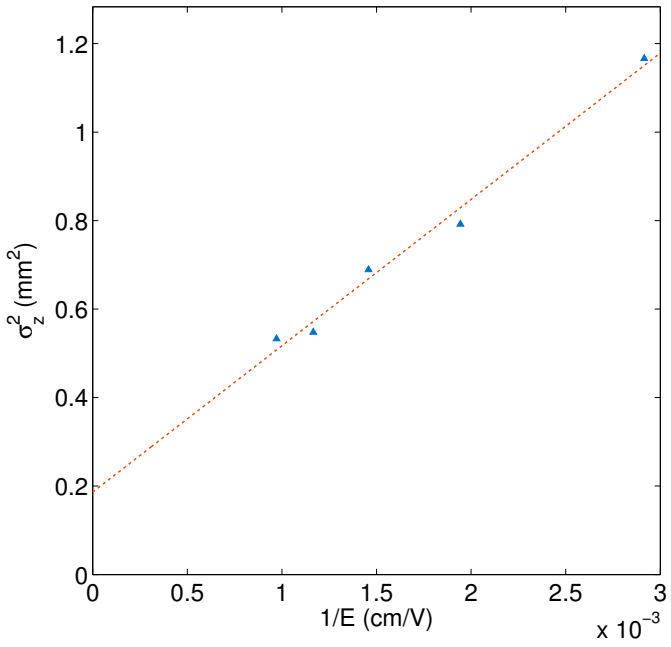

(a) CS_2 40 Torr

Figure 8

Table 1: Diffusion widths and coefficients for 20-40 Torr SF_6 and 40 Torr CS_2 at $E = 1029$ V/cm and $L = 58.3$ cm. The corrected σ_z (third column) is derived by subtracting the estimated $\sigma_{\text{other}} = 0.43 \pm 0.12$ mm, in quadrature, from the measured σ_z (second column).

Pressure [Torr]	σ_z [mm]	Corrected σ_z [mm]	D_L [cm^{2}s^{-1}]
20 SF_6	1.19	1.11	2.64
30 SF_6	0.85	0.73	0.76
40 SF_6	0.74	0.60	0.39
40 CS_2	0.73	0.59	0.29

0.34 mm. The upper bound due to the THGEM is determined by assuming a zero capture length, and this gives a value of 0.49 mm. It is by no coincidence that the thickness of the THGEM (0.4 mm) lies within this range while the THGEM pitch (0.5 mm) is close to the upper bound. The contribution from the field near the THGEM can be modeled, and the sum total of non-diffusion contributions can be determined by measuring the pulse-width as a function of drift distance. This is left for future work.

However, we can estimate in another way all contributions to the pulse width aside from diffusion by plotting σ_z^2 as a function of inverse of the electric field, $1/E$, as shown in Figure 8a for the 40 Torr CS_2 data. Since σ_z^2 is proportional to $1/E$, in the limit that $E \to \infty$, diffusion goes to zero and the vertical-intercept in Figure 8a gives the value of the square of the other contributions, σ_{other}^2, that are independent of electric field. We fit the data points in Figure 8a to a linear curve and obtained a value of $\sigma_{\text{other}} = 0.43 \pm 0.12$ mm, which is very close to our previous estimate of the THGEM field contribution to pulse width. The slope of the fit in Figure 8a gives a temperature of 330 ± 25 K for 40 Torr CS_2 and nearly the same value for 40 Torr SF_6, both consistent with room temperature. The corrected σ_z's are shown in the third column of Table 1 while the fourth column contains the corresponding diffusion coefficients. It is worth noting that the validity of applying the 40 Torr data correction value to the 30 and 20 Torr data is questionable as the systematics due to electron capture length and THGEM field effects are likely reduced field dependent.

A similar treatment of the SF_6 data would require fitting the pulses over a comparable range of E, but the non-Gaussian shape of the signals at low E prevents this. Nevertheless, the similar values of σ_z for SF_6 and CS_2 at 40 Torr (Table 1) suggest that the diffusion behavior of the two gases are quite similar. But it should be noted that the assumption of thermal diffusion could break down at higher E/P. A possible indication of this is the observed rise in the reduced mobility with increasing reduced field shown in Figure 6. This has important consequences for directional dark matter experiments where the requirement of both long drift distances and low diffusion can be met if thermal diffusion extends to the highest drift fields possible. This requires further investigations left for future work.

6. Gas Gain

Previous works have shown that gas gains greater than 1000 can be achieved in electronegative gases with proportional wires [56], GEMs [57], and bulk Micromegas (Micro Mesh Gaseous Structure) [58]. In contrast to electron gases where only moderate electric fields of order 100 V $cm^{-1}Torr^{-1}$ are needed to accelerate electrons to energies close to the ionization potential of the gas, electronegative gases require much higher electric fields to initiate avalanche even though the electron affinity is usually much lower than the ionization potential [59]. The reason for this lies in the difficulty of initiat-

ing the avalanche by detaching the electron from the negative ion, which is thermally coupled to the gas. For CS_2, measurements show that the pressure reduced minimum field, $E_{\rm min}/P$, needed to initiate avalanche is over one order of magnitude larger than for the electron drift gas P10 (10% Methane in Argon) [59]. A similar study can be done for SF_6, but in this section we omit a discussion of the detailed mechanism for avalanche in this gas and instead focus on the gas gains that were achieved.

The gas gain in SF_6 is measured with the use of an ^{55}Fe 5.89 keV X-ray source. To convert the energy of the X-ray into the number of electrons produced during the ionization process, we make use of the W-factor, which is defined as the mean energy required to create a single electron-ion pair. For SF_6, this value has been measured using α particles [60] and a ^{60}Co γ source [61]. Those measurements give $W_\alpha = 35.45$ eV and $W_\gamma = 34.0$ eV, respectively. The slight disagreement is actually consistent with other measurements of W-factors which find that W_α exceeds $W_{\gamma,\beta}$ for molecular gases [62]. Because we are using an X-ray source, we will adopt the W-factor from Ref. [61], so the average number of primary electrons, N_p, created by an ^{55}Fe X-ray interaction in SF_6 is

$$N_p = \frac{E_{^{55}\rm Fe}}{W_\gamma} = \frac{5.89 \text{ keV}}{34.0 \text{ eV}} \simeq 173. \tag{21}$$

The effective gas gain is then given by,

$$G_{\rm eff} = \frac{N_{\rm tot}}{N_p}, \tag{22}$$

where $N_{\rm tot}$ is the total number of charges read out with the preamplifier. In general, $N_{\rm tot}$ is less than the total number of charges produced in the avalanche due to an imperfect efficiency for collecting the charges, hence, the measured gain is an effective and not an absolute value. In our case, we are essentially collecting all of the electrons produced in the avalanche, but there is an additional contribution to the pulse shape from the positive ions that are also produced. To determine $N_{\rm tot}$ from a measured pulse's V(t), the standard calibration procedure of injecting a known charge into the preamplifier is used. In this case, we used an ORTEC 448 Research Pulser to inject charge into the 1 pF calibration capacitor inside the ORTEC 142 preamplifier.

For each pressure, we raised the GEM voltage until highly energetic sparks are observed and/or until the rate of micro-sparks and background events

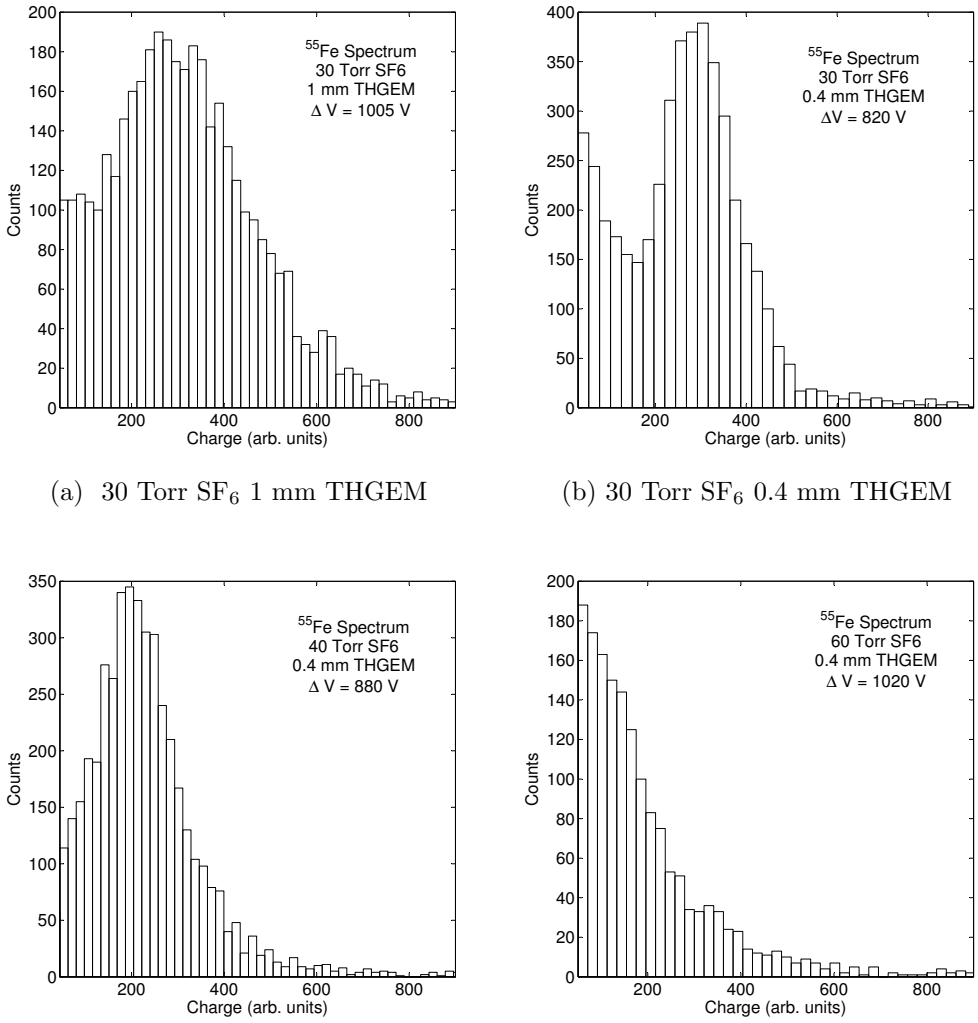

(a) 30 Torr SF_6 1 mm THGEM

(b) 30 Torr SF_6 0.4 mm THGEM

(c) 40 Torr SF_6 0.4 mm THGEM

(d) 60 Torr SF_6 0.4 mm THGEM

Figure 9: ^{55}Fe spectra in several pressures of SF_6 obtained using 1 mm and 0.4 mm THGEMs.

approach that of the ^{55}Fe source. In Figure 9, we show the ^{55}Fe energy spectra taken in SF_6 for several different pressures at a drift field of 500 V cm^{-1} using a 0.4 mm THGEM, as well as one taken with a 1 mm THGEM in 30 Torr. The 30 Torr spectra taken with the two different thicknesses

THGEM show distinctly different shapes. The 1 mm spectrum (Figure 9a) is much broader than the 0.4 mm spectrum (Figure 9b). In addition to the different shapes of the spectra, one also notices that the spectra are not Gaussians. There appears to be an extra exponential component alongside the potential peak in each of Figures 9a - 9c, and in Figure 9d, only an exponential component is detected. The exponential components in Figures 9a - 9c are the result of micro-sparks and background events. Nevertheless, these are not the only contribution to the 60 Torr spectrum as there is a clear rate difference above the trigger threshold when the ^{55}Fe source is switched on and off. At 20 and 100 Torr, we also detected a rate difference above trigger threshold but a spectrum was not taken due to instability.

At present, we do not have a clear explanation for the spectral shape differences in the 30 Torr data between the two THGEMs or the exponential shape of the 60 Torr data. One possible explanation for the peculiar spectral shapes in the 60 Torr data is that only a fraction of the negative ions created from the initial ^{55}Fe ionization event are accelerated to a sufficient energy for electron detachment to occur in avalanche region. However, many other complex processes occurring in this high field region such as the potential re-capture of the freed electrons by SF_6 or its sub-species (e.g. F, F_2, SF_4) which are produced as by-products of collisional avalanche could also play a role. The degradation of energy resolution due to electron capture in a high field region is a phenomenon that has been observed in CF_4, normally an electron drift gas, [63]. We leave this as an open question for future studies.

To better identify the background and signal components and quantify their shapes, we fitted the spectra from Figures 9a - 9c. The fit is composed of a Gaussian signal component, and an exponential and uniform background component. The fitted total spectrum and the individual signal and background components are shown in Figure 10 for the 30 Torr data taken using the 1 mm THGEM. The reduced chi-square (χ^2/ndf) of the fit is 1.29. The mean of the Gaussian corresponds to an effective gas gain of about 3000 while the energy resolution, σ/E, is 45% (106% FWHM).

For the 30 Torr data taken with the 0.4 mm THGEM, the the fits done in the same way are shown in Figure 11. The reduced chi-square (χ^2/ndf) of the fit is 1.26 and, similar to the 1 mm THGEM data, the mean of the Gaussian component corresponds to an effective gas gain of about 3000. But despite the data being taken at the same pressure and gas gain, the energy resolution, σ/E, for the 0.4 mm THGEM is 25% with the FWHM energy resolution being 58%. The difference in energy resolution could be

due to dissimilar amplification field strengths, which would effect the process of stripping the electron and possible subsequent reactions. The 1 mm THGEM is operated at a voltage of 1005 V while the 0.4 mm THGEM is operated at a voltage of 820 V, both at close to their maximum values beyond which unacceptable sparking levels occur. The electric field, E_{GEM}, inside the THGEM is approximately given by $\Delta V/d$, where d is the thickness of the GEM. For the 1 mm and 0.4 mm THGEMs, $E_{\mathrm{GEM}} = 10.05$ kV cm^{-1} and $E_{\mathrm{GEM}} = 20.50$ kV cm^{-1}, respectively. In addition to fluctuations in gas gain due to the electron detachment mean-free-path, the avalanche process in SF_6 may suffer from a competition with recapture on SF_6 or its fragments produced in the THGEM holes. As the cross-sections for attachment, dissociation, and ionization of SF_6 and its fragments are dependent on the energy of the electron, the distinctive spectral shapes and energy resolutions that we observe must originate from the difference of reduced electric field in the avalanche region and its influence on those processes.

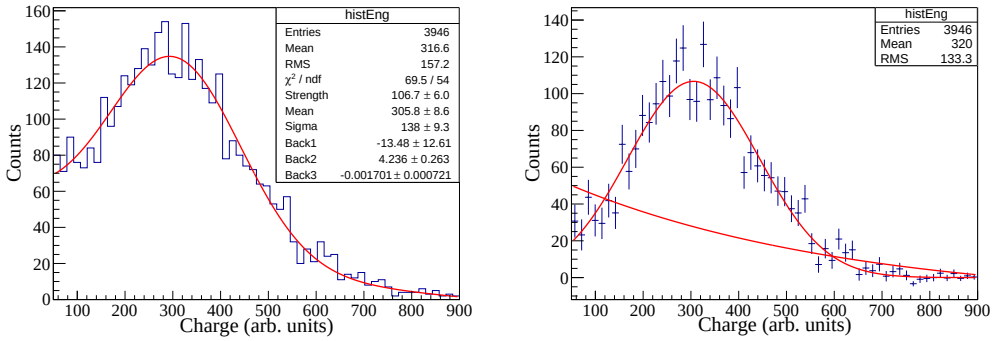

(a) ^{55}Fe energy spectrum in 30 Torr SF_6 using 1 mm THGEM

(b) ^{55}Fe energy spectrum after background subtraction.

Figure 10

Finally, shown Figure 12 are the same fits done for the 40 Torr data with a reduced chi-square for the fit of 1.66. The mean of the Gaussian in Figure 12b corresponds to a gain of about 2000 and its width corresponds to an energy resolution, σ/E, of 42% (FWHM 99%). The resolution is very similar to that of the 30 Torr, 1 mm THGEM data. The 40 Torr data, however, is taken with the 0.4 mm THGEM operated at a voltage of 880 V. This would imply an amplifying field of ~ 22.0 kV cm^{-1}, nearly the same strength as the

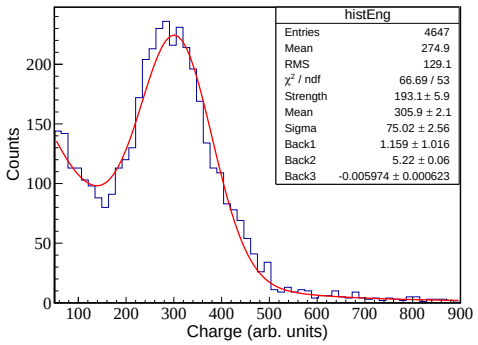

(a) ^{55}Fe energy spectrum in 30 Torr SF_6 using 0.4 mm THGEM

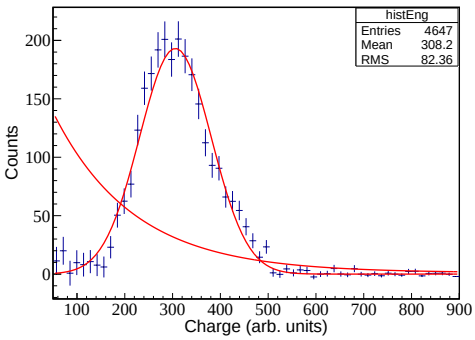

(b) ^{55}Fe energy spectrum after background subtraction.

Figure 11

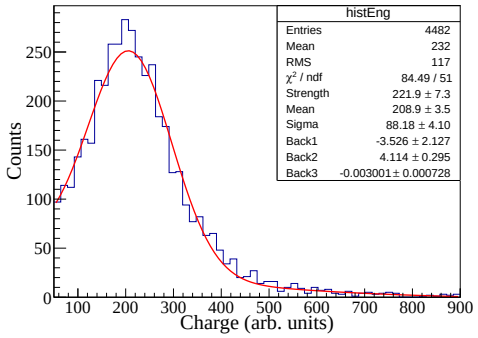

(a) ^{55}Fe energy spectrum in 40 Torr SF_6 using 0.4 mm THGEM

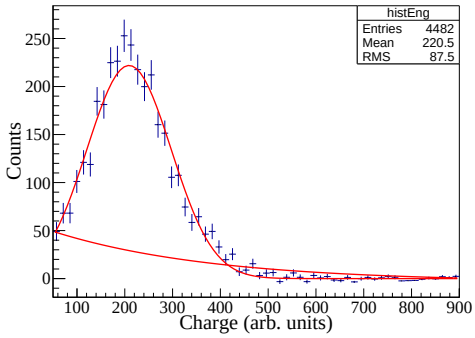

(b) ^{55}Fe energy spectrum after background subtraction.

Figure 12

30 Torr data taken with the 0.4 mm. Why then is the 40 Torr data not similar to the 30 Torr data taken with the 0.4 mm THGEM? Although the electric fields are similar, the reduced fields, E/p, are not, and the energies of the electrons in the avalanche region depend on the latter. The reduced field in the 30 Torr data taken with the 0.4 mm THGEM is 683 V cm^{-1}Torr^{-1} while in the 40 Torr data, the reduced field is 550 V cm^{-1}Torr^{-1}. This could also explain why the 60 Torr data taken at a reduced field of 425 V cm^{-1}Torr^{-1} showed no peak (Figure 9d). The peak in that spectrum could have fallen

below the trigger threshold because its width is so wide that only events on the right side of the peak are being recorded. If that is the case, we should be able to see the entire peak as we did in the 1 mm THGEM 30 Torr data by pushing the gain up much higher. However, we were not able to accomplish this with a single THGEM due to onset instability, but it could be possible with the addition of a second THGEM. In addition, if the reduced field in the avalanche region is influencing the width of the energy spectrum, could other avalanche devices that operate at much high reduced fields such as thin GEMs or Micromegas give better energy resolutions, provided that the gain is sufficiently high enough? This could be an interesting question for future studies.

7. Event Fiducialization Using Secondary Peak

We showed in Figure 2 of Section 3 that at high drift fields, the waveform of the charge arriving at the anode consists mainly of the two SF_5^- and SF_6^- peaks. Having two or more species of charge carriers with differing mobilities is critical for event fiducialization in gas-based TPCs employed in dark matter and other rare event searches. The ability to fiducialize in these experiments allows identification and removal of the most pernicious backgrounds, which originate at or near to the inner surfaces of the detector. Although identifying the event location in the readout plane (X,Y) of a TPC is trivial, locating the event along its drift direction (Z) is much harder. Unlike in accelerator-based experiments, the time of interaction (T^*) in a gas-based TPC used for rare searches is not available, so, until recently, Z-fiducialization had proven difficult. The recent discovery of minority charge carriers in CS_2 + O_2 mixtures [48], has changed this by allowing the differences in their mobility to be used to derive the Z of the event. This has transformed the DRIFT dark matter experiment [5], which has operated for close to a decade with irreducible backgrounds from radon progeny recoils from the TPC cathode [51, 52, 53, 54, 55]. The differences in the SF_5^- and SF_6^- mobilities in pure SF_6 mixtures can be used in a similar manner to measure the Z location of the event:

$$Z = \frac{v_s \cdot v_p}{v_s - v_p} \Delta T, \tag{23}$$

where v_p and v_s are the drift speeds of the negative ions in the primary (SF_6^-) and secondary (SF_5^-) peaks, respectively, and ΔT is the time separation of the peaks.

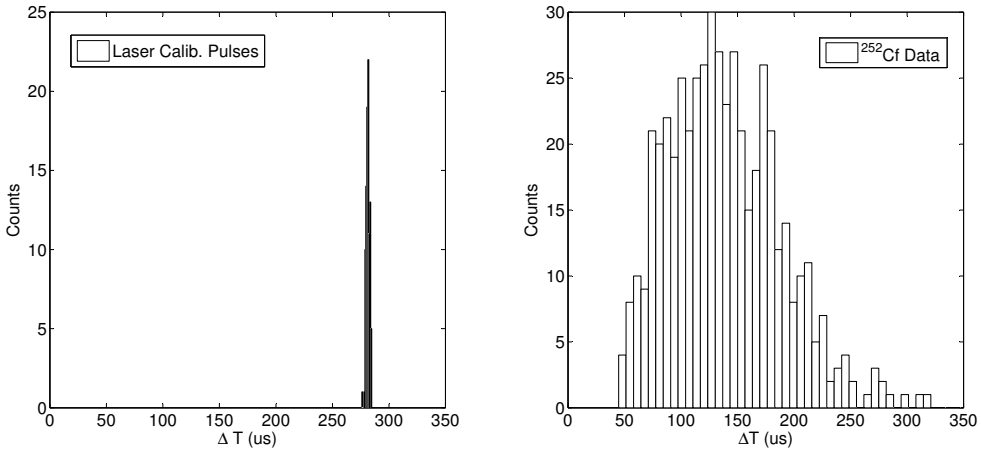

(a) Laser (b) ^{252}Cf

Figure 13: (a) Distribution of the time difference between secondary, SF_5^-, and primary, SF_6^- peaks (ΔT) for the laser calibration pulses obtained at 30 Torr SF_6 and $E = 1029$ V/cm. (b) The same distribution for the ^{252}Cf data which shows that the secondary peak is not a laser artifact.

To test how well one can determine the location of events using this method, we used a ^{252}Cf source to generate ionization events at different locations in the detection volume. The ^{252}Cf source was placed near the outside surface of the vessel and about 20 cm from the cathode. The detector was operated at 30 Torr with $E = 1029$ V/cm where the highest gas gains were achieved (Section 6). This was important for identifying the small SF_5^- peak in low energy recoils, which produce lower ionization than the nitrogen laser. Preceding the ^{252}Cf run, an energy calibration was done with an internally mounted ^{55}Fe source. In addition, we pulsed the laser onto the cathode to generate ionization at a known, $Z = 58.3$ cm, location to calibrate the into an absolute Z location.

The peaks are found through an automated process, rather than manually, using a derivative based peak finding algorithm. Although the algorithm performs efficiently for a large data set, the derivative based approach will tend to give false peak detections for noisy data. To reject events with false peak detections, we only accept events that have two and only two identified peaks, one corresponding to SF_5^- and the other to SF_6^-. This, of course,

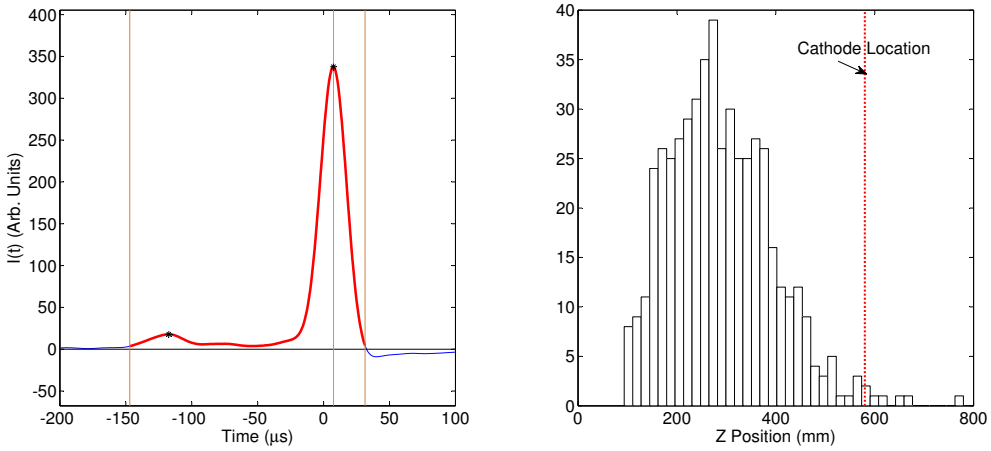

(a) A ^{252}Cf event. (b) ^{252}Cf Z distribution.

Figure 14: (a) An event from the ^{252}Cf run at 30 Torr SF_6 and $E = 1029$ V/cm which shows two distinct peaks. The black markers identify the locations of the peaks while the vertical lines on the two ends show the edges of the track. The single vertical line passing through the black marker passes through the location of the primary, SF_6^-, peak. (b) The distribution of the Z locations of events from the ^{252}Cf run after the peak number and energy cut. The vertical line shows the position of the cathode at Z = 58.3 cm. The events with Z locations greater than the cathode location are those that misidentified peaks.

will greatly reduce the efficiency of our analysis, but our aim here is only to demonstrate the possibility of event fiducialization in SF_6. Increasing the efficiency for acceptance of events requires a much better peak detection algorithm and is beyond the scope of this work. In addition to the cut that rejects events with more than two detected peaks, we reject events with an energy < 60 keVee (electron equivalent energy). Only higher energy events are accepted so that the SF_5^- peaks are more easily identified and also to reduce electronic recoils due to the gamma-rays from the source.

A sample event from the run with a relatively well-defined SF_5^- peak is shown in Figure 14a and demonstrates that the secondary peak phenomenon is most definitely not a laser artifact. The distribution of the time difference, ΔT, between the SF_5^- and SF_6^- peaks for the laser calibration data is shown in Figure 13a and has a mean of 281 μs and FWHM of about 26 μs (4 mm). The distribution of the same timing parameter from the ^{252}Cf run is shown in Figure 13b. The wide ΔT distribution from the ^{252}Cf run post cuts shown

in Figure 13b indicate that the time difference between the SF_5^- and SF_6^- is correlated with the location of the events in the detector and holds promise for their fiducialization. We also show the position distribution of events in Figure 14b, which is the result of converting the ΔT's into Z locations by using the laser calibration data. The Z distribution and its peak at ~ 30 cm is consistent with the larger solid angle intersecting the detector volume on the side of the anode. There are also no events seen for $Z < 10$ cm because the SF_5^- peak has merged into the primary SF_6^- peak and these events are rejected by the analysis.

An important question is can we increase the relative abundance of the SF_5^- to SF_6^- peak? Motivated by the behavior of the minority peaks in CS_2 and O_2 [48], we decided to add small amounts (< 1 Torr to a few Torr) of O_2 into SF_6, but no significant change in behavior was observed other than a small change in drift velocity and pulse width due to a change in E/p. An alternative approach is to increase the electric field beyond the current maximum value of 1029 V/cm. As noted in Section 3, the SF_5^-/SF_6^- ratio should increase with electron energy based on the cross-sections for both SF_5^- and SF_6^- [28, 29, 32]. However, there we showed no detectable change in the ratio when the drift field was raised from ~ 500 to ~ 1000 V/cm. Significantly higher drift fields may be needed to see a change but, even if these can be achieved at low pressures, we may enter a regime where non-thermal diffusion and large electron attachment mean free paths begin to deteriorate the track quality.

Interestingly, there exists a possible alternative approach to increasing the production of SF_5^- in SF_6. A study of the temperature dependence of SF_5^- production over the range 300 K to 880 K have shown that the first peak at ~ 0.0 eV is very sensitive to temperature with the relative cross-section for the formation of SF_5^- increasing by about two orders of magnitude over this temperature range at ~ 0.0 eV while the second broad peak at 0.38 eV is relatively independent of temperature variation [49]. This strong increase in the production cross-section for SF_5^- from SF_6 with temperature, and hence, the vibrational and rotational excitation energy of the SF_6 molecule led Ref.[49] to explore the potential for photo-enhancement of SF_5^- production via the processes:

$$\mathrm{n}(\mathrm{h}\nu)_{\mathrm{laser}} + \mathrm{SF}_6 \rightarrow (\mathrm{SF}_6^*)_{\mathrm{laser}} \tag{24}$$

$$(\mathrm{SF}_6^*)_{\mathrm{laser}} + \mathrm{e} \rightarrow (\mathrm{SF}_5^-)_{\mathrm{laser}} + \mathrm{F}. \tag{25}$$

Using a CO_2 laser ($9.4 - 10.6\ \mu$m) to vibrationally excite SF_6 molecules, they observed an enhancement of SF_5^- production that was radiation wavelength dependent and different for ^{32}S and ^{34}S isotopes. It should be noted that infrared excitation should not result in photodetachment of the SF_6^- anion as measurements have shown that the threshold for this process is at 3.16 eV (392 nm) [50]. However, because it is mainly the cross-section at 0.0 eV that is enhanced with an increase in temperature, it is unclear whether this idea will work for electrons in the high drift field of a TPC. Another important question is whether the diffusive behavior of the photo-excited gas would be affected. These are experimental questions that require further investigation. The promise of SF_6 make it imperative to push the idea as far as we can take it.

8. Conclusion

We have shown that gas gain is achievable in a low pressure gas detector with SF_6 as the bulk gas. Signals from low energy ^{55}Fe events were detected using a 0.4 mm and 1.0 mm THGEM with a gain of between 2000-3000 and energy resolution that appears to depend on the reduced field in the amplification region, implying that electron attachment could be the reason for this behavior. Testing other GEM geometries and amplification devices in SF_6 to achieve even better gain and energy resolution could be the subject for future work. The discovery of many interesting features in SF_6, particularly the waveform behavior with electric field and pressure, was made using a laser ionization generating system with, crucially, an acrylic cylindrical detector design that allowed for high reduced field operation. We have found the appearance of a second negative ion peak at high reduced fields which most likely corresponded to SF_5^-. Using the secondary peak, we showed that fiducializing events in the drift direction is possible. However, our diffusion measurements showed a large unaccounted for systematic but indicated that at 40 Torr, SF_6 has a similar diffusion width to CS_2, a gas already shown to have thermal diffusive behavior. There were many features of SF_6 found in this work that remain unexplained as a consequence of the design of our detector and experimental apparatus, which limited our ability to investigate each of those features in more detail. Nonetheless, these remaining mysteries should provide ample motivation and opportunities for future studies on the use of SF_6 in TPCs.

Acknowledgements

This material is based upon work supported by the NSF under Grant Nos. 1103420 and 1407773.

[1] L. G. Christophorou, J. K. Olthoff, and D. S. Green, NIST Technical Note 1425 (1997).

[2] L. G. Christophorou and J. K. Olthoff, J. Phys. Chem. Ref. Data, Vol. 29, No. 3 (2000).

[3] P. Camarri et al., Nucl. Instr. and Meth A 414 (1998) 317.

[4] G. Aielli et al., Nucl. Instr. and Meth A 493 (2002) 137.

[5] J. B. R. Battat et al., "First background-free limit from a directional dark matter experiment: results from a fully fiducialised DRIFT detector" , Phys. Dark Univ. 910(2015)17.

[6] L. G. Christophorou and J. K. Olthoff, Int. J. Mass Spectr. 205 (2001) 27.

[7] E.P. Grimsrud, S. Chowdhury, P. Kebarle, J. Chem. Phys. 83 (1985) 1059.

[8] E.C.M. Chen, J.R. Wiley, C.F. Batten, W.E. Wentworth, J. Phys. Chem. 98 (1994) 88.

[9] S. J. Cavanagh, S. T. Gibson, and B. R. Lewis, J. Chem. Phys. 137, 144304 (2012).

[10] NIST Standard Reference Database 69: NIST Chemistry WebBook.

[11] J. Ellis and R. A. Flores, Phys. Lett. B 263, 259 (1991).

[12] C. J. Martoff et al., Nucl. Instrum. Methods Phys. Res. A 440, 355 (2000).

[13] L. G. Christophorou, "Insulating Gases," Nuclear Instruments and Methods in Physics Research, Vol. A268, pp. 424-433, 1988.

[14] L. G. Christophorou and S. R. Hunter, "From Basic Research to Applications", in Electron-Molecule Interactions and Their Applications, L. G. Christophorou (Ed.), Academic Press, NY, Vol. 2, Chap. 5, 1982.

[15] Th. Aschwanden, "Swarm Parameters in SF6 and SFe/N2 Mixtures Determined from a Time Resolved Discharge Study", in Gaseous Dielectrics IV, L. G. Christophorou and M. 0. Pace (Eds.), Pergamon Press, NY, pp. 24-32, 1984.

[16] D. Edelson, J. E. Griffiths, and K. B. McAfee, Jr., J. Chem. Phys. 37,917 (1962).

[17] R. N. Compton, L. G. Christophorou, G. S. Hurst, and P. W. Reinhardt, J. Chem. Phys. 45, 4634 (1966).

[18] P. W. Harland and J. C. J. Thynne, J. Phys. Chem. 75, 3517 (1971).

[19] L. G. Christophorou, *Atomic and Molecular Radiation Physics* (Wiley, New York, 1971), Ch. 6.

[20] L. G. Christophorou, Adv. Electron, Electron Phys. 46, 55 (1978).

[21] L. G. Christophorou, D. L. McCorkle, and A. A. Christodoulides, Electron-Molecule Interactions and Their Applications, edited by L. G. Christophorou (Academic, New York, 1984), Vol. 1, Chap. 6.

[22] J. M. S. Henis and C. A. Mabie, J. Chem. Phys. 53, 2999 (1970).

[23] R. W. Odom, D. L. Smith, and J. H. Futrell, J. Phys. B 8, 1349 (1975).

[24] M. S. Foster and J. L. Beauchamp, Chem. Phys. Lett. 31, 482 (1975).

[25] E. W. McDaniel, E. A. Mason, The Mobility and Diffusion of Ions in Gases, John Wiley & Sons, USA, 1973

[26] B. Lehmann, Z. Naturforsch. 25A (1970) 1755.

[27] M. V. V. S. Rao, S. K. Srivastava, in: T. Andersen, B. Fastrup, F. Folkmann, H. Knudsen (Eds.), Proceedings of the 18th International Conference on the Physics of Electronic and Atomic Collisions, Aarhus, Denmark, July 2127, 1993, Abstracts of contributed papers, p. 345.

[28] L. E. Kline, D. K. Davies, C. L. Chen, P. J. Chantry, J. Appl. Phys. 50 (1979) 6789.

[29] L. G. Christophorou and J. K. Olthoff, Int. J. Mass Spectrom., 205 (2001) 2741.

[30] H. Hotop, D. Klar, J. Kreil, M.-W. Ruf, A. Schramm, J. M. Weber, in: L. J. Dube, J. B. A. Mitchell, J. W. McConkey, C. E. Brion (Eds.), The Physics of Electronic and Atomic Collisions, AIP Conference Proceedings, vol. 360, AIP Press, Woodbury, New York, 1995, p. 267.

[31] D. Klar, M.-W. Ruf, H. Hotop, Aust. J. Phys. 45 (1992) 263.

[32] S. R. Hunter, J. G. Carter, L. G. Christophorou, J. Chem. Phys. 90 (1989) 4879.

[33] X. Ling, B. G. Lindsay, K. A. Smith, F. B. Dunning, Phys. Rev. A 45 (1992) 242.

[34] P. L. Patterson, J. Chem. Phys. 53, 696 (1970).

[35] J. de Urquijo-Carmona, I. Alvarez, H. Martinez, and C. Cisneros, J. Phys. D 24, 664 (1991).

[36] I. A. Fleming and J. A. Rees, J. Phys. B: At. Mol. Phys. 2 777-9 (1969).

[37] Y. Wang, R. L. Champion, L. D. Doverspike, J. K. Olthoff, and R. J. van Brunt, J. Chem. Phys. 91, 2254, (1989).

[38] A. A. Christodoulides, D. L. McCorkle, and L. G. Christophorou, in *Electron-Molecule Interactions and Their Applications*, edited by L. G. Christophorou (Academic, New York, 1984), Vol. 2, Chap. 6.

[39] J. K. Olthoff, R. J. van Brunt, Y. Wang, R. L. Champion, and L. D. Doverspike, J. Chem. Phys. 91, 2261, (1989).

[40] R. L. Champion, in *Gaseous Dielectrics VI*, edited by L. G. Christophorou and I. Sauers, (Plenum, New York, 1991), p. 1.

[41] D. P. Snowden-Ifft and J.-L. Gauvreau Rev. Sci. Instrum. 84, 053304 (2013).

[42] Y. Nakamura, J. Phys. D: Appl. Phys. 21 (1988) 67-72.

[43] F. Li-Aravena and M. Saporoschenko, J. Chem. Phys. 98, 11 (1993).

[44] J. de Urquijo-Carmona, I. Alvarez, C. Cisneros, and H. Martinez, J. Phys. D: Phys. 23 (1990) 778-783.

[45] W. Blum and L. Rolandi, "Particle Detection with Drift Chambers", New York: Springer-Verlag (1994).

[46] E. A. Mason and E. W. McDaniel, *Transport Properties of Ions in Gases* (Wiley, New York, 1988).

[47] L. A. Viehland and E. A. Mason, Atomic Data and Nuclear Data Tables 60, 37-95 (1995).

[48] D. P. Snowden-Ifft, Rev. Sci. Instrum. 85, 013303 (2014).

[49] C. L. Chen and P. J. Chantry, J. Chem. Phys. 71 (1979) 3897.

[50] P. G. Datskos, J. G. Carter, an L. G. Christophorou, Chem. Phys. Lett. 239, 38 (1995).

[51] S. Burgos et al., Astroparticle Physics, 28 (45) (2007), pp. 409421

[52] J. Brack et al., JINST 9 P07021 (2014).

[53] J. B. R. Battat et al., JINST 9 P11004 (2014).

[54] J. B. R. Battat et al., Nucl. Instr. Meth. Phys. Res. A 794 (2015) 3346.

[55] J. Brack et al., Phys. Procedia 61 (2015) 130137.

[56] D. P. Snowden-Ifft et al., Neutron recoils in the DRIFT detector, Nucl. Instr. Meth. A 498 (13) (2003) 155164.

[57] J. Miyamoto et al., GEM operation in negative ion drift gas mixtures, Nucl. Instr. Meth. A 526 (2004) 409412.

[58] I. Giomataris, R. De Oliveira, S. Andriamonje, S. Aune, G. Charpak, P. Colas, G. Fanourakis, E. Ferrer, A. Giganon, Ph. Rebourgeard, P. Salin, Micromegas in a bulk, Nucl. Instr. Meth. A 560 (2006) 405408.

[59] M. P. Dion, C. J. Martoff, and M. Hosack, Astroparticle Physics 33 (2010) 216220.

[60] Y. H. Hilal and L. G. Christophorou, J. Phys. D: Appl. Phys. 20 (1987).

[61] I. Lopes, H. Hilmert, and W. F. Schmidt, J. Phys. D: Appl. Phys. 19 (1986).

[62] L. G. Christophorou, "Atomic and Molecular Radiation Physics", New York: Wiley-Interscience (1971).

[63] W. S. Anderson, J. C. Armitage, E. Dunn, J. G. Heinrich, C. Lu, K. T. McDonald, J. Weckel and Y. Zhu, Nucl. Instr. Meth. A 323 (1992) 273-279.